

Testing planet formation from the ultraviolet to the millimeter

Nick Choksi¹* and Eugene Chiang^{1,2}

¹*Astronomy Department, Theoretical Astrophysics Center, and Center for Integrative Planetary Science, University of California Berkeley, Berkeley, CA 94720, USA*

²*Department of Earth and Planetary Science, University of California, Berkeley, CA 94720, USA*

Released 1 December 2021

ABSTRACT

Gaps imaged in protoplanetary discs are suspected to be opened by planets. We compute the present-day mass accretion rates \dot{M}_p of seven hypothesized gap-embedded planets, plus the two confirmed planets in the PDS 70 disc. The accretion rates are based on disc gas surface densities Σ_{gas} from C¹⁸O observations, and planet masses M_p from simulations fitted to observed gaps. Assuming accretion is Bondi-like, we find in eight out of nine cases that \dot{M}_p is consistent with the time-averaged value given by the current planet mass and system age, M_p/t_{age} . As system ages are comparable to circumstellar disc lifetimes, these gap-opening planets may be undergoing their last mass doublings, reaching final masses of $M_p \sim 10 - 10^2 M_{\oplus}$ for the non-PDS 70 planets, and $M_p \sim 1 - 10 M_J$ for the PDS 70 planets. For another fifteen gaps without C¹⁸O data, we predict Σ_{gas} by assuming their planets are accreting at their time-averaged \dot{M}_p . Bondi accretion rates for PDS 70b and c are orders of magnitude higher than accretion rates implied by measured U-band and H α fluxes, suggesting most of the accretion shock luminosity emerges in as yet unobserved wavebands, or that the planets are surrounded by dusty, highly extinguishing, quasi-spherical circumplanetary envelopes. Thermal emission from such envelopes or from circumplanetary discs, on Hill sphere scales, peaks at wavelengths in the mid-to-far-infrared and can reproduce observed mm-wave excesses.

Key words: planets and satellites: formation – planets and satellites: general – planets and satellites: fundamental parameters – protoplanetary discs – planet–disc interactions

1 INTRODUCTION

The Atacama Large Millimeter Array (ALMA) has revealed gaseous protoplanetary discs to be ringed and gapped, with HL Tau (ALMA Partnership et al. 2015) and discs from the DSHARP (Andrews et al. 2018) and MAPS (Oberg et al. 2021) surveys providing stunning examples (see also Cieza et al. 2019; Andrews 2020). The annular structures observed at orbital distances of $r \sim 10 - 100$ au are commonly interpreted as being carved by protoplanets within the gaps, by analogy with shepherd satellites opening gaps in planetary rings (e.g. Goldreich & Tremaine 1979). A few dozen candidate planets have been so hypothesized with masses M_p of several Earth masses M_{\oplus} to a few Jupiter masses M_J (Zhang et al. 2018; figure 1 of Lodato et al. 2019; and Table 1 of this paper).

So far disc-embedded protoplanets have been directly imaged in one system: PDS 70b and c are confirmed in the near-infrared to orbit at $r \sim 20 - 40$ au within the central clearing of the system’s transitional disc (Keppler et al. 2018; Haffert et al. 2019; Wang et al. 2020, 2021, and references therein). These protoplanets, each estimated to be of order a Jupiter mass, have been imaged at multiple wavelengths, from the ultraviolet at 336 nm (Zhou et al. 2021) to H α (Haffert et al. 2019) to the sub-millimeter continuum (Isella et al. 2019; Benisty et al. 2021). Aside from PDS 70b and c, all other planets proposed to explain disc sub-structures remain undetected. There are unconfirmed near-infrared point sources in HD 163296

(Guidi et al. 2018) and Elias 24 (Jorquera et al. 2021), and kinematical evidence for planetary perturbations to the rotation curve in HD 163296 (Teague et al. 2018, 2021).

Are the disc gaps and rings imaged by ALMA and in the infrared (e.g. Asensio-Torres et al. 2021) really caused by planets? What can we hope to learn from DSHARP discs and similar systems about how planets form? At the top of the list of measurables should be the planetary mass accretion rate \dot{M}_p and how it depends on M_p and ambient disc properties like density and temperature. The planet masses inferred from modeling disc sub-structures are frequently dozens of Earth masses (e.g. Dong & Fung 2017; Zhang et al. 2018; our Table 1),¹ large enough that an order-unity fraction of their mass should be in the form of accreted hydrogen. For such planets with self-gravitating gas envelopes, accretion may be hydrodynamic, i.e. regulated by how much mass the surrounding nebula can deliver to the planet through transonic/supersonic flows (e.g. D’Angelo et al. 2003; Machida et al. 2010; Tanigawa & Tanaka 2016; Ginzburg & Chiang 2019a). This phase is distinct from an earlier thermodynamic phase of gas accretion limited by the rate at which the nascent envelope can cool and contract quasi-hydrostatically (e.g. Lee & Chiang 2015; Ginzburg et al. 2016; Chachan et al. 2021). Are the inferences of planets still immersed in their parent discs consistent with our ideas

¹ The gaps simulated by Zhang et al. (2018) and similar works are opened because of the repulsive Lindblad torques exerted by planets. These planet-disk simulations neglect accretion onto the planet (cf. Rosenthal et al. 2020 and references therein).

* E-mail: nchoksi@berkeley.edu

of hydrodynamic accretion? To what final masses should we expect the hypothesized planets to grow?

This paper takes stock of the developing landscape of disc sub-structures and directly imaged protoplanets to address these and other questions. Our goal is to assess what we have learned (if anything) about planet formation from the multi-wavelength observations, and how theory fares against data. In these early days, the analysis is necessarily at the order-of-magnitude level. We begin in Section 2 by documenting our sources (mostly DSHARP) for disc and putative planet properties. These quantities are used in Section 3 to estimate the present-day \dot{M}_p according to theory and to evaluate whether the corresponding planet growth timescales M_p/\dot{M}_p make sense in comparison to the system ages. The mass accretion rates are also used to evaluate accretion luminosities, and we discuss how accretion may be playing out in the circumplanetary environments of PDS 70b and c. In Section 4, we summarize and offer an outlook.

2 OBSERVATIONAL DATA

Table 1 compiles disc and candidate planet properties taken directly from the literature or derived therefrom. Quantities of interest include the host stellar mass M_\star and planet mass M_p , the gas and dust surface densities Σ_{gas} and Σ_{dust} at planet orbital distance r , and the local disc aspect ratio h/r . To the nineteen DSHARP protoplanets modeled by Zhang et al. (2018) we add the one candidate protoplanet in HD 169142 (Dong & Fung 2017), the two candidates in TW Hya (Dong & Fung 2017), and the two confirmed planets in PDS 70 (Keppler et al. 2018; Haffert et al. 2019).

2.1 Gas surface densities Σ_{gas}

We focus on systems for which emission from optically thin C^{18}O has been spatially resolved. More abundant isotopologues of CO are usually optically thick (including ^{13}CO ; van der Marel et al. 2015; Favre et al. 2019) and as such yield only lower limits on Σ_{gas} . Hydrogen surface densities derived from C^{18}O emission are nonetheless uncertain. The gas-phase $\text{CO}:\text{H}_2$ abundance ratio X_{CO} is hard to determine; it may be lower in protoplanetary discs than in the interstellar medium (ISM) because of condensation of CO onto dust grains or chemistry driven by cosmic rays (e.g. Schwarz et al. 2018). We will try to account for the possibility of gas-phase CO depletion in what follows. Surface densities at the centers of gaps where planets supposedly reside may also be overestimated if gaps are spatially underresolved, with emission from gap edges contaminating the emission at gap center. Such contamination might not be too serious for the gaps considered in this subsection, whose radial widths are larger (marginally) than the corresponding ALMA beams. Also, simulations predict gas density variations less than a factor of 10 across gaps for $M_p \lesssim 60 M_\oplus$ (e.g. Dong et al. 2017, top left panel of their figure 8).

Of the twenty-four planets in our sample we have measurements of Σ_{gas} based on C^{18}O emission (in conjunction with other emission lines) for nine planets in six systems.

2.1.1 Gas surface density: AS 209

The protoplanetary disc around AS 209 has five annular gaps in dust continuum emission at orbital radii $r \approx 9, 24, 35, 61,$ and 99 au (Guzmán et al. 2018; Huang et al. 2018). Zhang et al. (2018) demonstrated that the four gaps from $24 - 99$ au can be produced by a single planet situated within the outermost gap at 99 au (see their

figure 19). Favre et al. (2019) and Zhang et al. (2021) observed a broad gap in C^{18}O (2-1) emission extending from ~ 60 to 100 au. Favre et al. (2019) modeled the emission using the DALI thermochemical code (Bruderer 2013) and took the gas density profile to include two gaps coincident with the dust gaps at 61 and 99 au. They showed these two gas gaps could be smeared by the ALMA beam into a single wide gap like that observed in molecular emission. At the bottom of the 99 au gap where the planet is believed to reside, they fitted $\Sigma_{\text{gas}} \approx 0.04 - 0.08 \text{ g/cm}^2$ (see the blue and green curves in their figure 6).

Zhang et al. (2021) modeled the C^{18}O emission using the thermochemical code RAC2D (Du & Bergin 2014), including only a single gap. They initialized their models with an ISM-like X_{CO} which decreased from CO freeze-out and chemistry over the simulation duration of 1 Myr. They found $\Sigma_{\text{gas}} \approx 0.08 \text{ g/cm}^2$ at 99 au (their figure 16), similar to Favre et al. (2019). Zhang et al. (2021) also considered the possibility that there is no gap in H_2 and that the observed gap in C^{18}O is due to X_{CO} being somehow locally depleted beyond the predictions of RAC2D. Assuming a total gas-to-dust ratio of 10 by mass (their table 2), they estimated in this super-depleted X_{CO} scenario $\Sigma_{\text{gas}} \approx 0.4 \text{ g/cm}^2$ at 99 au (their figure 5; see also Alarcón et al. 2021 who advocated on separate grounds for a depleted $\text{CO}:\text{H}_2$ ratio in AS 209).

We combine the results of Favre et al. (2019) and Zhang et al. (2021) to consider $\Sigma_{\text{gas}} = 0.04 - 0.4 \text{ g/cm}^2$ for the gap AS 209-G2 at $r = 99$ au (Table 1).

2.1.2 Gas surface density: HD 163296

Dust continuum observations of HD 163296 reveal gaps centred at $10, 48,$ and 86 au (Isella et al. 2016; Huang et al. 2018), each opened by a separate planet according to Zhang et al. (2018). Isella et al. (2016) fitted the emission at $r \gtrsim 25$ au from three CO isotopologues assuming an ISM-like value of X_{CO} and found $\Sigma_{\text{gas}} \approx 2.5 - 10 \text{ g/cm}^2$ at 48 au and $\Sigma_{\text{gas}} \approx 0.1 - 2 \text{ g/cm}^2$ at 86 au (their figure 2, blue curve; note the gap radii in their figure are about 20% larger than the values we use because they used a pre-GAIA source distance). The thermochemical models of Zhang et al. (2021) predict roughly consistent values of $\Sigma_{\text{gas}} \approx 1 \text{ g/cm}^2$ and $\Sigma_{\text{gas}} \approx 0.6 \text{ g/cm}^2$ respectively (see their figure 16). If instead the $\text{CO}:\text{H}_2$ abundance is much lower than predicted by their models and the gas-to-dust ratio is 60 (their table 2), then $\Sigma_{\text{gas}} \approx 40 \text{ g/cm}^2$ and $\Sigma_{\text{gas}} \approx 20 \text{ g/cm}^2$ (their figure 5).

The above estimates of Σ_{gas} are combined to yield the full ranges quoted in Table 1, $\Sigma_{\text{gas}} = 1 - 40 \text{ g/cm}^2$ for HD 163296-G2 at 48 au, and $\Sigma_{\text{gas}} = 0.1 - 20 \text{ g/cm}^2$ for HD 163296-G3 at 86 au.

2.1.3 Gas surface density: IM Lup

IM Lup presents a shallow gap at $r \approx 117$ au in millimeter continuum images (Huang et al. 2018) which Zhang et al. (2018) attributed to a $10\text{-}30 M_\oplus$ planet. Zhang et al. (2021) found $\Sigma_{\text{gas}} \approx 0.1 \text{ g/cm}^2$ in their RAC2D modeling which includes CO freeze-out and chemistry (their figure 16). Alternatively, for a super-depleted $\text{CO}:\text{H}_2$ scenario and gas-to-dust ratio of 100 (their table 2), $\Sigma_{\text{gas}} \approx 10 \text{ g/cm}^2$ (their figure 5). We allow for both possibilities and take $\Sigma_{\text{gas}} = 0.1 - 10 \text{ g/cm}^2$.

2.1.4 Gas surface density: HD 169142

HD 169142 features an annular gap at 50 au in near-infrared scattered light (Quanz et al. 2013) and mm-wave continuum emission (Fedele et al. 2017). In C^{18}O emission, Fedele et al. (2017) found

(1) Name	(2) $M_{\star} [M_{\odot}]$	(3) $t_{\text{age}} [\text{Myr}]$	(4) $r [\text{au}]$	(5) $M_{\text{p}} [M_{\oplus}]$	(6) $\Sigma_{\text{gas}} [\text{g cm}^{-2}]$	(7) $\Sigma_{\text{dust}} [\text{g cm}^{-2}]$	(8) h/r
Sz 114	0.17	1	39	3 – 6	N/A	0.08 – 0.6	0.1
GW Lup	0.46	2	74	2 – 10	N/A	0.03 – 0.2 [†]	0.08
Elias 20	0.48	≤ 0.8	25	8 – 20	N/A	0.1 – 0.7	0.08
Elias 27	0.49	0.8	69	3 – 20	N/A	0.05 – 0.3	0.09
RU Lup	0.63	0.5	29	10 – 20	N/A	0.2 – 1	0.07
SR 4	0.68	0.8	11	60 – 700	N/A	0.03 – 0.2 [†]	0.05
Elias 24	0.78	0.2	57	30 – 300	N/A	0.003 – 0.02	0.09
TW Hya-G1	0.80	8	21	8 – 80	0.04 – 3	0.06 – 0.4	0.08*
TW Hya-G2	0.80	8	85	5 – 50	0.008 – 0.2	0.002 – 0.02	0.09*
Sz 129	0.83	4	41	5 – 10	N/A	0.2 – 1	0.06
DoAr 25-G1	0.95	2	98	20 – 30	N/A	0.05 – 0.3	0.07
DoAr 25-G2	0.95	2	125	5 – 10	N/A	0.08 – 0.6	0.07
IM Lup	1.1	0.5	117	10 – 30	0.1 – 10	0.03 – 0.2	0.1*
AS 209-G1	1.2	1	9	60 – 700	N/A	0.05 – 0.3 [†]	0.04
AS 209-G2	1.2	1	99	30 – 200	0.04 – 0.4	0.008 – 0.06	0.06*
HD 142666	1.58	10	16	10 – 100	N/A	0.2 – 1	0.05
HD 169142	1.65	10	51	30 – 300	0.1 – 0.2	≤ 0.01	0.07*
HD 143006-G1	1.78	4	22	400 – 6000	N/A	0.003 – 0.02 [†]	0.04
HD 143006-G2	1.78	4	51	20 – 100	N/A	0.02 – 0.2	0.05
HD 163296-G1	2.0	10	10	30 – 200	N/A	0.2 – 1	0.07*
HD 163296-G2	2.0	10	48	90 – 700	1 – 40	0.003 – 0.02 [†]	0.08*
HD 163296-G3	2.0	10	86	10 – 300	0.1 – 20	0.01 – 0.09	0.08*
PDS 70b	0.88	5	22	300 – 3000	0.0008 – 0.08	≤ 0.02	0.07*
PDS 70c	0.88	5	34	300 – 3000	0.0008 – 0.08	≤ 0.02	0.08*

Table 1. Properties of gapped discs and the planets hypothesized to reside within them (confirmed in the case of PDS 70). Column headings: (1) System name. For systems with multiple gaps, we append “G#” to distinguish between different gaps. (2) Stellar mass (Andrews et al. 2018; Ducourant et al. 2014; Oberg et al. 2021; Blondel & Djie 2006; Keppler et al. 2019) (3) Stellar age (Andrews et al. 2018; Ducourant et al. 2014; Pohl et al. 2017; Müller et al. 2018) (4) Planet orbital radius (Zhang et al. 2018; Dong & Fung 2017; Keppler et al. 2018) (5) Planet mass. For the non-PDS 70 planets (first 22 entries), the quoted range in M_{p} corresponds to disc viscosities $\alpha = 10^{-5} - 10^{-3}$, scaled from the gap-fitting, two-fluid, planet-disc simulations of Zhang et al. (2018) and Dong & Fung (2017) (see section 2.4.1). The ranges on M_{p} for PDS 70b and c roughly cover values inferred from infrared photometry and cooling models (Müller et al. 2018; Keppler et al. 2018; Wang et al. 2020). (6) Gas surface density at the planet’s location, as inferred from C^{18}O emission (Nomura et al. 2021; Zhang et al. 2021; Favre et al. 2019; Fedele et al. 2017; Isella et al. 2016; Facchini et al. 2021). The quoted ranges on Σ_{gas} in AS 209, IM Lup, HD 163296, and TW Hya accommodate the possibility that the $\text{CO}:\text{H}_2$ abundance ratio in these discs is lower than in the ISM (Zhang et al. 2019; Calahan et al. 2021; Zhang et al. 2021). (7) Dust surface density at the planet’s location (Huang et al. 2018; Nomura et al. 2021; Fedele et al. 2017; Benisty et al. 2021) accounting for an assumed factor of 7 uncertainty in opacity. Because most gaps are only marginally resolved in mm continuum emission we are likely overestimating Σ_{dust} (see section 2.2). Daggers (†) mark the five gaps which Jennings et al. (2021) found to have lower dust continuum intensities and hence lower Σ_{dust} than Huang et al. (2018) found. (8) Disc aspect ratio, mostly taken from Zhang et al. (2018) except for those marked with an asterisk (see section 2.3). The values for t_{age} , M_{p} , Σ_{gas} , Σ_{dust} , and h/r are uncertain and quoted to only one significant figure.

evidence for a cavity inside $r \approx 50$ au and used DALI to infer $\Sigma_{\text{gas}} \approx 0.1 - 0.2 \text{ g/cm}^2$ near the cavity outer edge (their figure 5, top left panel, blue curve). Midplane gas temperatures according to the same thermo-chemical model (figure 5, bottom center panel) are $\sim 30 - 40$ K, higher than the CO freeze-out temperature of ~ 20 K. CO may still be depleted for other reasons (Schwarz et al. 2018) but without a model we cannot quantify the uncertainty.

2.1.5 Gas surface density: TW Hya

Near-infrared scattered light images reveal annular gaps at $r \approx 21$ au (TW Hya-G1) and 85 au (TW Hya-G2) (van Boekel et al. 2017). The inner gap may also have been detected in the mm continuum by Andrews et al. (2016), albeit slightly outside the gap in scattered light (their figure 2). Nomura et al. (2021) studied TW Hya in the $J = 3 - 2$ transition of C^{18}O . Near the inner gap they measured a wavelength-integrated line flux of $5 \text{ mJy beam}^{-1} \text{ km s}^{-1}$ (their figure 2, middle panel, orange curve). We extrapolate their radial intensity profile, which cuts off at 80 au, to the outer gap at 85 au and estimate there a flux of $1 \text{ mJy beam}^{-1} \text{ km s}^{-1}$. Using temperatures of 60 K

and 20 K for the inner and outer gaps respectively (section 2.3.3), we convert these fluxes to C^{18}O column densities (e.g. Mangum & Shirley 2015, their equation B2). Then assuming $X_{\text{CO}} = 10^{-4}$ and a $^{18}\text{O}:\text{O}$ gas-phase abundance ratio of 2×10^{-3} (e.g. Qi et al. 2011), we calculate $\Sigma_{\text{gas}} = 0.04 \text{ g/cm}^2$ and 0.008 g/cm^2 for the two gaps. These surface densities could be underestimated by factors of 70 and 30 (assuming a gas-to-dust ratio of 100), respectively, if CO is somehow super-depleted (Zhang et al. 2019, their figure 8, second panel, blue curve). Thus we have $\Sigma_{\text{gas}} \approx 0.04 - 2.8 \text{ g/cm}^2$ for TW Hya-G1 and $\Sigma_{\text{gas}} \approx 0.008 - 0.24 \text{ g/cm}^2$ for TW Hya-G2.

2.1.6 Gas surface density: PDS 70

Facchini et al. (2021) studied PDS 70 in the $J = 2 - 1$ transition of C^{18}O , but the beam size at this wavelength was too large to resolve the cavity within which the two planets reside. We therefore resort to using the C^{18}O emission just outside the cavity to place an upper limit on the gas surface density near the planets. Following the same procedure as for TW Hya, we convert the observed C^{18}O flux outside the cavity into an H_2 surface density. We use 30 K as

the gas excitation temperature at 80 au, close to the H_2CO excitation temperature measured by [Facchini et al. \(2021\)](#), their figure 7). The gas surface density so derived is $\Sigma_{\text{gas}} = 8 \times 10^{-2} \text{ g/cm}^2$. We pair this upper limit with a lower limit derived from optically thick ^{12}CO in the $J = 3 - 2$ transition. The smaller beam associated with the higher frequency of this transition allowed the cavity to be resolved by [Facchini et al. \(2021\)](#). Near the positions of the planets at $r \sim 22 - 34$ au, the observed ^{12}CO line flux is 37 K km s^{-1} , which for an assumed temperature of $T \sim 60 \text{ K}$ (scaled from 30 K at 80 au using $T \propto r^{-3/7}$ for a passively irradiated disk; [Chiang & Goldreich 1997](#)) yields a lower bound on Σ_{gas} of $8 \times 10^{-4} \text{ g/cm}^2$. The temperatures quoted above are high enough to avoid CO freeze-out, though we cannot rule out that gas-phase CO is depleted from other effects ([Schwarz et al. 2018](#)).

2.2 Dust surface densities Σ_{dust}

The dust surface density Σ_{dust} and the dust optical depth τ (typically evaluated at mm wavelengths) are related by

$$\Sigma_{\text{dust}} = \frac{\tau}{\kappa}. \quad (1)$$

The opacity κ depends on the grain size distribution. We allow κ to range from 0.4 to 3 cm^2 per gram of dust,² following model size distributions by [Birnstiel et al. \(2018\)](#) which include grains up to 1 cm in size. For a given temperature T , we infer τ from the specific intensity I_ν :

$$I_\nu = B_\nu(T) (1 - e^{-\tau}) \quad (2)$$

where $B_\nu(T)$ is the Planck function.

Surface densities may be overestimated inside gaps that are spatially underresolved. This may be a much more serious problem for Σ_{dust} than for Σ_{gas} (cf. section 2.1) because simulations predict dust surface densities to vary by orders of magnitude across gaps carved by $M_{\text{p}} \gtrsim 10 M_{\oplus}$ planets, with dust gradients steepened by aerodynamic drag (e.g. figure 1 of [Paardekooper & Mellema 2004](#); figure 8 of [Dong et al. 2017](#); figure 4 of [Binkert et al. 2021](#)). We caution that the values of Σ_{dust} we derive may therefore be grossly overestimated. See also [Jennings et al. \(2021\)](#), whose work we describe below.

2.2.1 Dust surface density: DSHARP systems

For all nineteen of the DSHARP planets, we estimate Σ_{dust} at gap center using equation (1) and the optical depth profiles in figure 6 of [Huang et al. \(2018\)](#).

Three of the DSHARP gaps, AS 209-G2 ($r = 99$ au), Elias 24 (57 au), and HD 143006-G1 (22 au), have bottoms that fall below the 2σ noise floor at $\tau = 10^{-2}$, although apparently only marginally so. For Elias 24 and HD 143006-G1, we set $\tau = 10^{-2}$. For AS 209-G2, while portions of the gap lie below the noise floor, at gap center there is actually a local maximum (ring) of emission that rises above the noise. We use the peak optical depth of this ring, $\tau \approx 2 \times 10^{-2}$, to evaluate Σ_{dust} . The “W”-shaped gap profile for AS 209-G2 resembles transient structures found in two-fluid simulations of low-mass planets embedded in low-viscosity discs ([Dong et al. 2017](#); [Zhang et al. 2018](#)).

² The ALMA continuum data used in our study were taken at wavelengths ranging from 0.85 mm to 1.27 mm. Our adopted factor-of-seven uncertainty in κ is larger than the expected variation of κ across this wavelength range (at fixed grain size), so for simplicity we ignore the wavelength dependence on κ when computing Σ_{dust} from the ALMA observations.

In their re-analysis at higher spatial resolution of the DSHARP data, [Jennings et al. \(2021\)](#), their figure 12) found evidence for deeper dust gaps than originally measured by [Huang et al. \(2018\)](#) for GW Lup, HD 163296-G2, SR 4, AS 209-G1, and HD 143006-G1. The re-analyzed gaps in the mm continuum are deeper by at least a factor of 10 and in most cases much more. We make a note of these sources in Table 1, but continue to use the [Huang et al. \(2018\)](#) results to compute Σ_{dust} for consistency with the rest of our analysis.

2.2.2 Dust surface density: TW Hya

For TW Hya-G1 at 21 au we calculate $\Sigma_{\text{dust}} = 0.06 - 0.4 \text{ g/cm}^2$ using equations (1)-(2) with $I_\nu = 10 \text{ mJy beam}^{-1}$ (figure 2, middle panel, purple curve of [Nomura et al. 2021](#)) and $T = 60 \text{ K}$ (section 2.3.3). For TW Hya-G2 at 85 au we estimate $\Sigma_{\text{dust}} = 0.002 - 0.02 \text{ g/cm}^2$ using $I_\nu \sim 10^{-1} \text{ mJy beam}^{-1}$ (this is an extrapolation of the intensity profile measured by [Nomura et al. 2021](#) which does not extend beyond ~ 70 au) and $T = 20 \text{ K}$. Our estimates of Σ_{dust} are consistent with those plotted in figure 3 of [Nomura et al. \(2021\)](#).

2.2.3 Dust surface density: HD 169142 and PDS 70

For the gap in HD 169142 and central clearing in PDS 70, the continuum emission falls below the 3σ noise floor of the observations ($0.21 \text{ mJy beam}^{-1}$ and $0.0264 \text{ mJy beam}^{-1}$, respectively; [Fedele et al. 2017](#); [Benisty et al. 2021](#)). For assumed temperatures of $T = 40 \text{ K}$ in HD 169142 and $T = 60 \text{ K}$ in PDS 70, the corresponding upper limits on the dust column are $\Sigma_{\text{dust}} \leq 10^{-2} \text{ g/cm}^2$ and $\Sigma_{\text{dust}} \leq 2 \times 10^{-2} \text{ g/cm}^2$, respectively.

2.3 Disc scale height h

2.3.1 Disc scale height: DSHARP systems

For most of the DSHARP sample, we adopt the h/r estimates listed in table 3 of [Zhang et al. \(2018\)](#), computed assuming a passive disc irradiated by its host star. For AS 209-G2, all three gaps in HD 163296, and IM Lup, we use more sophisticated estimates of h/r from table 2 of [Zhang et al. \(2021\)](#). In AS 209, [Zhang et al. \(2021\)](#) used the observed ^{13}CO emission surface to fit for $h/r = 0.06(r/100 \text{ au})^{0.25}$ (since their CO isotopologue data do not extend down to AS 209-G1 at 9 au, we only apply this scale height relation to AS 209-G2 at 99 au). Note that [Zhang et al. \(2018\)](#) found a similar value, $h/r = 0.05$ at 99 au, reproduced the multi-gap structure of AS 209. For HD 163296 and IM Lup, [Zhang et al. \(2021\)](#) obtained excellent fits to the spectral energy distributions (their figure 4) using $h/r = 0.084(r/100 \text{ au})^{0.08}$ and $h/r = 0.1(r/100 \text{ au})^{0.17}$, respectively.³

³ The values of h obtained by [Zhang et al. \(2021\)](#), if interpreted as a standard isothermal hydrostatic disc gas scale height, imply gas temperatures that differ from the gas temperatures obtained from thermo-chemical and radiative transfer modeling by these same authors (their figure 7). This is because the latter temperatures are solved assuming a fixed density field (specified by h), and no provision is made to iterate the density field to ensure simultaneous hydrostatic and radiative equilibrium. There is no rigorous justification for using either set of temperatures to compute the gas scale height; we use h as tabulated by [Zhang et al. \(2021\)](#) for convenience (their parameters H_{100} and ψ in table 2, inserted into their equation 3 with $\chi = 1$).

2.3.2 Disc scale height: HD 169142

Fedele et al. (2017) simultaneously fitted the surface density and temperature profiles in HD 169142. We use their aspect ratio of $h/r = 0.07$ at the gap position; this is similar to the value of $h/r = 0.08$ found by Dong & Fung (2017) in fitting the gap width to their planet-disk simulations. The aspect ratio relates to the disc midplane temperature following $h/r = c_s/(\Omega r)$ where $c_s = \sqrt{kT/\mu m_p}$ is the sound speed, $\mu = 2.4$ is the mean molecular weight, k is Boltzmann's constant, m_p is the proton mass, $\Omega = \sqrt{GM_\star/r^3}$ is the Keplerian orbital frequency, and G is the gravitational constant. The implied temperature at the gap position is 40 K.

2.3.3 Disc scale height: TW Hya

Calahan et al. (2021) obtained a good fit to the spectral energy of TW Hya using $h/r = 0.11 (r/400 \text{ au})^{0.1}$ (their figure 5). From this scaling we calculate $h/r = 0.08$ and $h/r = 0.09$ at the inner ($r = 21$ au) and outer ($r = 85$ au) gap positions, respectively. These aspect ratios correspond to temperatures of 58 K and 20 K.

2.3.4 Disc scale height: PDS 70

Absent direct estimates of the temperature in the PDS 70 cavity, we estimate the disc scale height using arguments similar to those in section 2.1.6. Facchini et al. (2021) derived an H₂CO excitation temperature near the disc midplane of 33 K at 80 au (see their figure 7). Setting this equal to the gas kinetic temperature there, we calculate $h = c_s/\Omega$ at 80 au, and then scale to the location of the planets assuming $h/r \propto r^{2/7}$ (Chiang & Goldreich 1997). We find $h/r = 0.07$ and 0.08 at the locations of PDS 70b and c. Keppler et al. (2018) found a similar temperature profile in their radiative transfer models of the PDS 70 disc.

2.4 Planet and stellar masses

2.4.1 Planet masses M_p and stellar masses M_\star : DSHARP systems

Zhang et al. (2018) used their grid of planet-disk hydrodynamical simulations to estimate the planet masses that can reproduce the radial widths and in some cases the radial positions of DSHARP gaps. Their table 3 gives M_p for different dust grain size distributions and the Shakura & Sunyaev (1973) viscosity parameter α . Here we consider $\alpha = 10^{-5} - 10^{-3}$. Values of $\alpha \gtrsim 10^{-2}$ appear incompatible with various mm-wave observations (Pinte et al. 2016; Teague et al. 2016; Flaherty et al. 2017) including the multi-gap structure of some discs (Dong et al. 2017; Zhang et al. 2018). Planet masses inferred by Zhang et al. (2018) increase with viscosity as $M_p \propto \alpha^{1/3}$; more massive planets are required to counteract faster diffusion of gas to open the same width gap. Thus to obtain an upper limit on M_p we use the entries corresponding to $\alpha = 10^{-3}$ in table 3 of Zhang et al. (2018), and for a lower limit we take their M_p values for $\alpha = 10^{-4}$ and divide by two in a crude extrapolation down to $\alpha = 10^{-5}$. This procedure gives a range on M_p that typically spans a factor of 8, and that encompasses the variation in M_p due to different dust size distributions.

For HD 163296-G3, we increase the upper bound on M_p to $1 M_J$ based on the fit to non-Keplerian kinematical data from Teague et al. (2018) and Teague et al. (2021). Note that their mass estimate is based on planet-disc simulations assuming $\alpha = 10^{-3}$, and that lowering α lowers the planet mass required to reproduce the same non-Keplerian velocity signature ($M_p \propto \alpha^{0.41}$ according to equation 16 of Zhang

et al. 2018). For Elias 24, the M_p range in Table 1 overlaps with mass estimates inferred from infrared photometry of an unconfirmed point source at $r \approx 55$ au (Jorquera et al. 2021). The candidate point source in HD 163296 is located at $r \approx 67$ au (Guidi et al. 2018) and as such cannot be identified with the planets inferred at $r \approx 48$ and 86 au (Zhang et al. 2018) of interest here.

For most of the DSHARP systems we use stellar masses derived from stellar evolution tracks and listed in table 1 of Andrews et al. (2018). For IM Lup, AS 209, and HD 163296 we use instead $M_\star = 1.2, 1.1,$ and $2.0 M_\odot$ respectively, calculated from gas disc rotation curves by Teague et al. (2021) as part of the MAPS survey (Oberg et al. 2021).

2.4.2 Planet and stellar masses: HD 169142 and TW Hya

By comparing the observed gaps in HD 169142 and TW Hya with their grid of planet-disk simulations, Dong & Fung (2017) estimated planet masses of $M_p = 0.2 - 2 M_J$ in HD 169142, $0.05 - 0.5 M_J$ in TW Hya-G1, and $0.03 - 0.3 M_J$ in TW Hya-G2. These values were derived for viscosities $\alpha = 10^{-4} - 10^{-2}$. For consistency with our adopted range of $\alpha = 10^{-5} - 10^{-3}$ (see section 2.4.1), we apply the same $M_p \propto \alpha^{1/3}$ scaling from Zhang et al. (2018) and shift all limits from Dong & Fung (2017) down by a factor of two.

The stellar masses of HD 169142 and TW Hya are $M_\star = 1.65 M_\odot$ and $M_\star = 0.8 M_\odot$, respectively (Blondel & Djie 2006; Ducourant et al. 2014).

2.4.3 Planet and stellar masses: PDS 70

Masses of PDS 70b and c derived from near-infrared spectral energy distributions and cooling models vary widely (Müller et al. 2018; Keppler et al. 2018; Christiaens et al. 2019; Mesa et al. 2019; Wang et al. 2020; Stolker et al. 2020). For simplicity we take $M_p = 1 - 10 M_J$ for both planets, which brackets most literature estimates relying on cooling models.⁴ This range is consistent with masses for PDS 70b derived by Wang et al. (2021) based on dynamical stability constraints. They calculated a 95% upper limit of $10 M_J$, with roughly equal probability per log mass from 1-10 M_J (see their figure 5).

The mass of the star is $M_\star = 0.88 M_\odot$ (Keppler et al. 2019).

3 PLANETARY ACCRETION RATES AND GAP PROPERTIES

Most of the gap-opening planets in our sample have inferred masses large enough that the self-gravity of their gas envelopes should be significant. In this regime, further accretion of gas from the disc may no longer be limited by Kelvin-Helmholtz cooling of the envelope but may instead be regulated by the hydrodynamics of the surrounding

⁴ In later sections, and in particular the discussion surrounding Figures 5 and 6, we will consider the possibility that the observed near-infrared emission does not arise from a planet passively cooling into empty space (as assumed by the cooling models) but one which sits below a hot accretion shock boundary layer. In this scenario our adoption of planetary masses for PDS 70b and c drawn from the passive cooling models will lead to an inconsistency. Our hope is that our estimated mass range of $1 - 10 M_J$ is not seriously impacted; it should not be as long as the posited accretion luminosities are not much larger than the observed near-infrared luminosities ($10^{-4} L_\odot$; Wang et al. 2020). It may also help to have the accretion columns be localized to “hot spots” on the planet, like they are for magnetized T Tauri stars (e.g. Gregory et al. 2006), leaving the rest of the planet passively cooling.

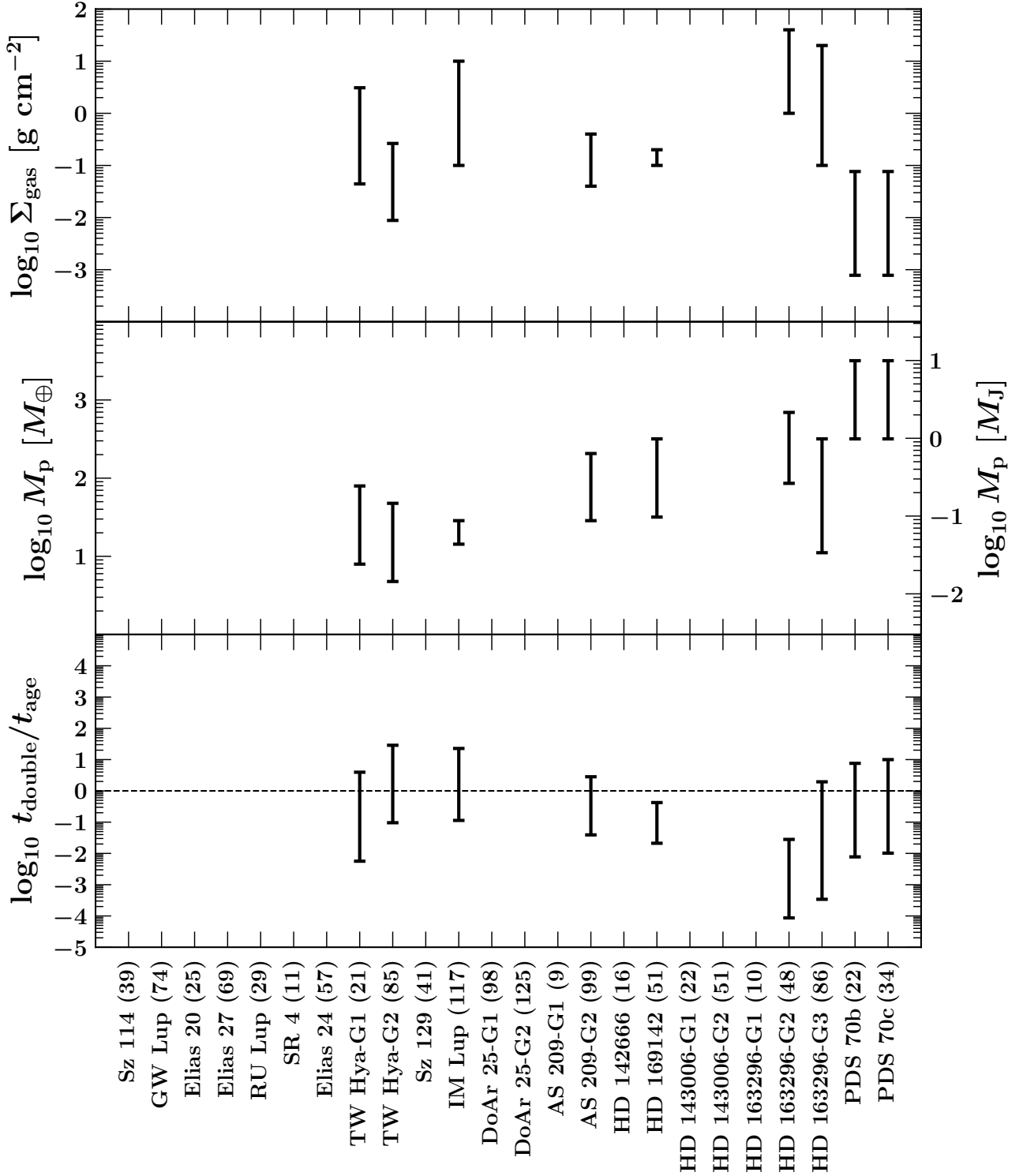


Figure 1. Top panel: Gas surface density Σ_{gas} at the centers of gaps hypothesized (confirmed for PDS 70) to host planets, for the subset of systems detected in C^{18}O . System names on the horizontal axis are followed by “G#” to identify a specific gap in systems with multiple gaps, and by the planet’s orbital radius r in units of au in parentheses. Systems are listed in order of increasing host stellar mass M_* , except for PDS 70 which as the only transitional disc in our sample is placed at the end. For TW Hya we estimate Σ_{gas} from the C^{18}O line flux (Nomura et al. 2021), while for AS 209, IM Lup, HD 169142, and HD 163296 Σ_{gas} derives from detailed thermo-chemical modeling (Favre et al. 2019; Zhang et al. 2021; Fedele et al. 2017; Isella et al. 2016). For PDS 70, we bound Σ_{gas} using the C^{18}O 2-1 flux outside the disc cavity and the ^{12}CO 3-2 flux inside the cavity (Facchini et al. 2021). **Middle panel:** Planet masses M_p . For the non-PDS 70 planets M_p is drawn from gap-fitting simulations by Zhang et al. (2018) and Dong & Fung (2017) scaled to viscosities $\alpha = 10^{-5} - 10^{-3}$. For PDS 70b and c, $M_p = 1 - 10 M_J$ roughly encompasses values from cooling models (e.g. Haffert et al. 2019). **Bottom panel:** Mass doubling times $t_{\text{double}} \equiv M_p / \dot{M}_p$ calculated assuming accretion at the Bondi rate (equation 3). Accretion rates \dot{M}_p are evaluated using Σ_{gas} and M_p as above, plus h and r compiled in Table 1. Error bars account for uncertainties in Σ_{gas} and M_p , with $t_{\text{double}} \propto 1 / (M_p \Sigma_{\text{gas}})$. Eight of the nine hypothesized planets may have t_{double} comparable to their system age t_{age} , a plausible result that if true suggests these planets are undergoing their last doublings.

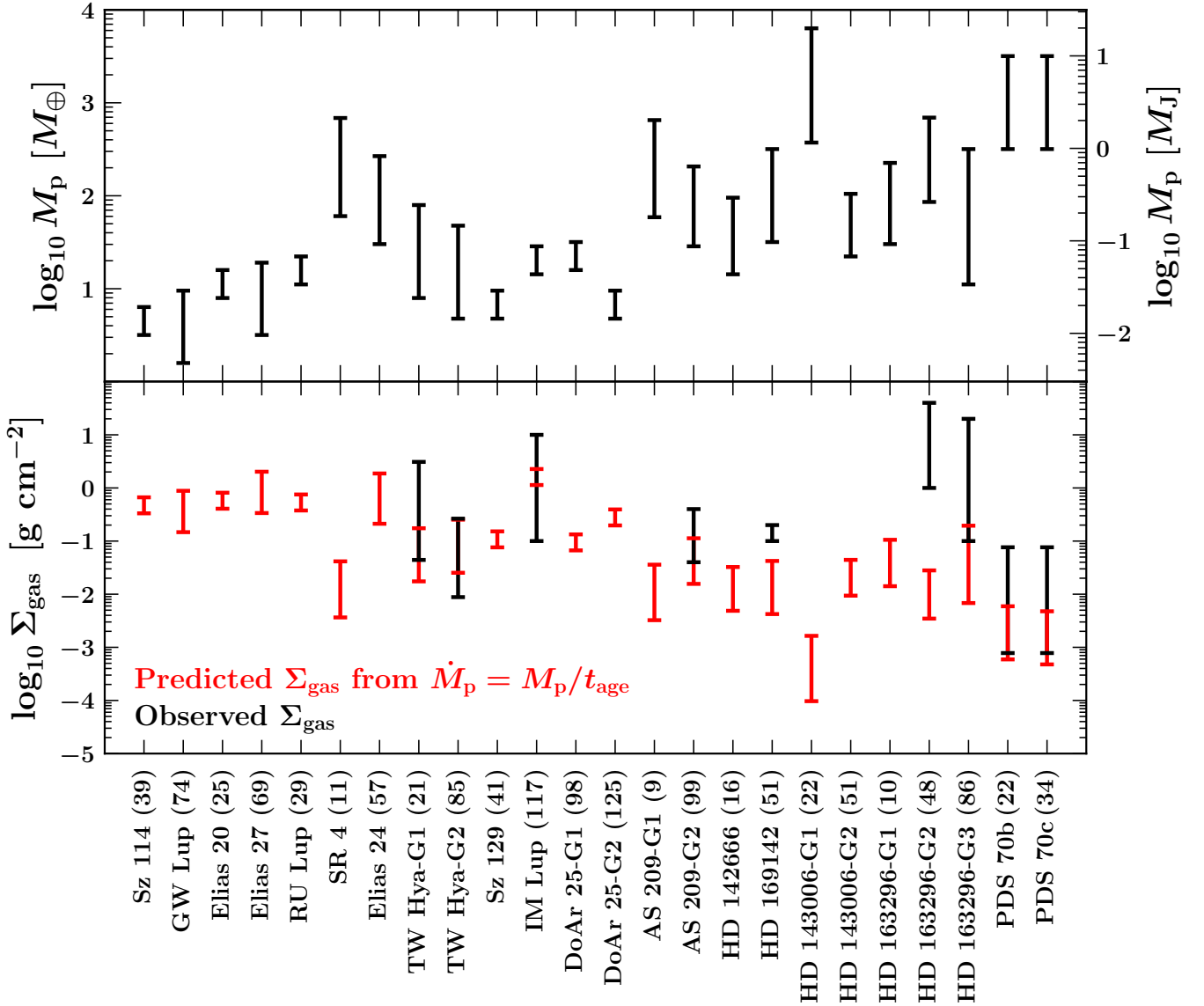


Figure 2. **Top panel:** Same as the middle panel of Figure 1, with M_p now plotted for all 24 planets in our sample. **Bottom panel:** Same as the top panel of Figure 1, with red points added to mark Σ_{gas} predicted from equation (5). The prediction assumes that each planet is accreting at the Bondi-like rate given by (3) and that $\dot{M}_p = M_p/t_{\text{age}}$ (equivalently $t_{\text{double}} = t_{\text{age}}$; for Elias 24 we use the upper limit on t_{age}). The last equality is motivated by the bottom panel of Figure 1. The evaluation of (5) uses M_p in the top panel plus r and h listed in Table 1. Red error bars reflect the range of M_p values considered.

nebula. Hydrodynamical forces include, in principle, pressure, planetary gravity, stellar tides, and rotation, all in 3D. The simplest form of hydrodynamical accretion is Bondi accretion, which describes spherically symmetric (zero angular momentum) flow onto a point mass (e.g. Frank et al. 2002). For a point mass embedded in a disc, the Bondi rate is given by:

$$\dot{M}_p = 0.25\Omega r^2 \left(\frac{M_p}{M_{\star}}\right)^2 \left(\frac{h}{r}\right)^{-4} \Sigma_{\text{gas}} \quad (3)$$

(e.g. Ginzburg & Chiang 2019a). While it ignores many effects, Bondi accretion appears to fit the results of 3D isothermal hydrodynamic simulations of accreting planets by D’Angelo et al. (2003), both in magnitude and in the M_p^2 scaling (see figure 1 of Tanigawa & Tanaka 2016 which re-prints their data). We have inserted in equation (3) a factor of 0.25 to match the normalization of the $\dot{M}_p \propto M_p^2$ relation measured by D’Angelo et al. (2003) at $M_p \lesssim 30 M_{\oplus}$. These

authors found that at higher masses, $\dot{M}_p(M_p)$ flattens away from an M_p^2 scaling; this flattening is due to the conflating effect of gap opening, i.e. Σ_{gas} in equation (3) decreases with M_p for masses $\gtrsim 30 M_{\oplus}$ as deeper gaps are opened. Note that the accretion rates measured by D’Angelo et al. (2003) may be sensitive to their mass removal prescription, which reduces the mass density inside the innermost $\sim 10\%$ of the planet’s Hill sphere by some fraction every simulation timestep. This prescription effectively renders the planet a sink cell and maximizes \dot{M}_p .

The corresponding planet mass doubling time is

$$t_{\text{double}} \equiv \frac{M_p}{\dot{M}_p}. \quad (4)$$

We test the theory of planet accretion (Bondi accretion) by comparing the doubling time t_{double} to the age of the system t_{age} . We expect $t_{\text{double}} \gtrsim t_{\text{age}}$. Steady and ongoing growth over the planet’s

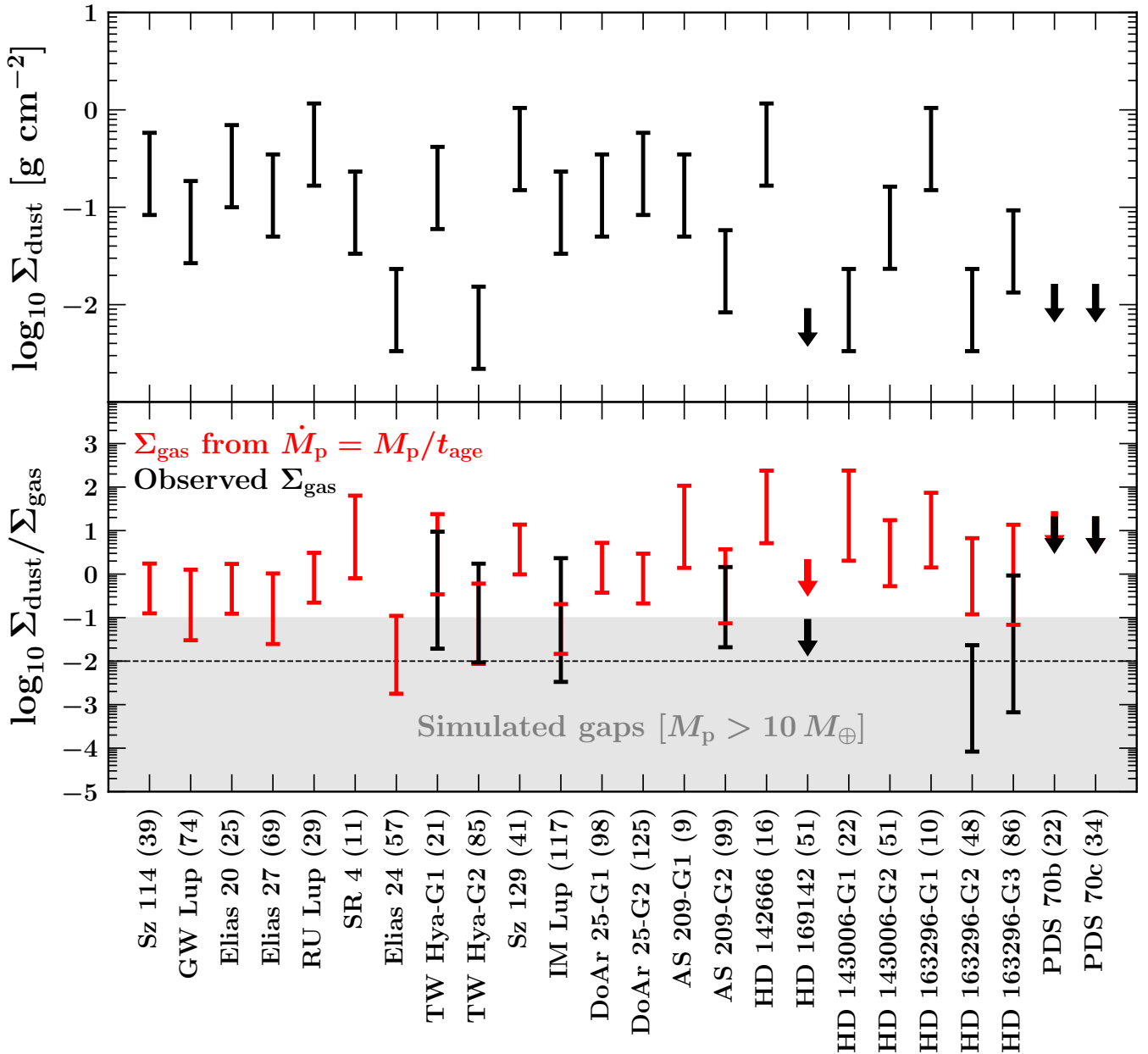


Figure 3. Top panel: Same as the top panel of Figure 1 but plotting dust surface densities Σ_{dust} inside gaps based on observed mm continuum intensities (Huang et al. 2018), assuming the dust is optically thin. Error bars account for a factor of seven uncertainty in the grain opacity but do not account for the limited spatial resolution of the observations which may lead to Σ_{dust} being overestimated. For HD 169142 and PDS 70, we plot upper limits on Σ_{dust} set by the noise floor of the observations (Fedele et al. 2017; Benisty et al. 2021). **Bottom panel:** Gap dust-to-gas ratios $\Sigma_{\text{dust}}/\Sigma_{\text{gas}}$. In black we combine the values of Σ_{dust} with Σ_{gas} inferred from C^{18}O intensity maps (Figure 1, top panel). In red we use the same Σ_{dust} data but take Σ_{gas} from equation (5), which presumes that planets accrete in a Bondi-like way with growth timescales \dot{M}_p/\dot{M}_p equal to system ages (Figure 2, red points). The shaded bar covers the range of dust-to-gas ratios found inside gaps opened by planets with $M_p > 10M_{\oplus}$ in two-fluid simulations by Dong et al. (2017). Many of the empirical data lie outside the simulated range, possibly because dust gaps are still underresolved by ALMA and therefore Σ_{dust} is overestimated. In support of this idea, Jennings et al. (2021) re-analyzed the DSHARP data and found deeper bottoms to the dust gaps in GW Lup, SR 4, AS 209-G1, HD 143006-G1, and HD 163296-G2.

age corresponds to $t_{\text{double}}/t_{\text{age}} \sim 1$ (equivalently $\dot{M}_p \sim M_p/t_{\text{age}}$). Alternatively, we may be observing the planet after it has largely finalized its mass, in which case $t_{\text{double}} > t_{\text{age}}$. We would not expect to find $t_{\text{double}} \ll t_{\text{age}}$ as a planet is unlikely to be caught in a short-lived episode of significant growth.

3.1 Bondi accretion rates \dot{M}_p from C^{18}O , and t_{double} vs. t_{age}

Figure 1 plots the ratio $t_{\text{double}}/t_{\text{age}}$ for each of the nine protoplanets with Σ_{gas} measured from C^{18}O observations (section 2.1). We find that $t_{\text{double}}/t_{\text{age}}$ appears in the majority of cases to be consistent with unity, although the error bars, which reflect the combined uncertainty in Σ_{gas} and M_p , are large. The result $t_{\text{double}}/t_{\text{age}} \sim 1$ is physically plausible and indicates that the planets are currently accreting at

rates \dot{M}_p close to the values time-averaged over their system ages, $\dot{M}_p \sim M_p/t_{\text{age}}$. For TW Hya-G1, AS 209-G2, HD 169142, and HD 163296-G3, $t_{\text{double}}/t_{\text{age}} \sim 1$ if $M_p \sim 10 - 30 M_{\oplus}$ and $\Sigma_{\text{gas}} \sim 0.1 \text{ g/cm}^2$, near the lower ends of their ranges in Table 1. Lower planet masses imply lower disc viscosities ($\alpha \sim 10^{-5}$) insofar as $M_p \propto \alpha^{1/3}$ (Zhang et al. 2018 and section 2.4.1). Lower gas surface densities argue against speculative super-depleted CO scenarios and support thermo-chemical models (DALI, Bruderer 2013; RAC2D, Du & Bergin 2014) that account for the usual ways that CO can be depleted, freeze-out and chemistry.

The gap HD 163296-G2 at $r = 48$ au does not meet our expectation that $t_{\text{double}}/t_{\text{age}} \gtrsim 1$. For this case the computed value of $t_{\text{double}}/t_{\text{age}} \lesssim 10^{-1}$ is driven by the large Jupiter-scale mass that Zhang et al. (2018) inferred from the observed deep and wide dust gap (Isella et al. 2016; Huang et al. 2018). Such a massive planet seems inconsistent with there being hardly any depression in the gas at this location (Zhang et al. 2021, their figure 16 and section 4.3.2). Rodenkirch et al. (2021) modeled the HD 163296 disc and found that a Jovian-mass planet at 48 au would deplete the gas density by a factor of ~ 10 for $\alpha = 2 \times 10^{-4}$ (their figure 5). We speculate that a planet much less massive than Jupiter might reproduce the dust and gas observations and bring t_{double} into closer agreement with t_{age} , if such a lower-mass planet caused only modest gas pressure variations that led to stronger dust variations via aerodynamic drift (Paardekooper & Mellema 2004; Dong et al. 2017; Drazkowska et al. 2019; Binkert et al. 2021). Another possibility is that there is no planet at all inside the HD 163296-G2 gap, as a planet can create gaps not centered on its orbit; figure 8 of Dong et al. (2018) explicitly models this scenario for HD 163296.

For PDS 70b and c, $t_{\text{double}}/t_{\text{age}} \sim 1$ implies $\dot{M}_p \sim 6 \times 10^{-7} - 6 \times 10^{-6} M_J \text{ yr}^{-1}$ assuming $M_p = 3 M_J$. These values are factors of 10-100 higher than estimates based on the observed U-band and H α fluxes (e.g. Haffert et al. 2019; Zhou et al. 2021). Section 3.3 discusses possible reasons why.

3.2 Σ_{gas} and Σ_{dust}

Fifteen of the twenty-four gaps in our sample lack published C¹⁸O data, precluding us from estimating Σ_{gas} and by extension \dot{M}_p . An alternate approach is to reverse the logic by first assuming that $\dot{M}_p \sim M_p/t_{\text{age}}$ (i.e. assuming $t_{\text{double}}/t_{\text{age}} \sim 1$), inserting this accretion rate into equation (3), and solving for Σ_{gas} :

$$\Sigma_{\text{gas}} = \frac{4M_p}{r^2} \frac{1}{\Omega t_{\text{age}}} \left(\frac{M_{\star}}{M_p} \right)^2 \left(\frac{h}{r} \right)^4 \quad \text{if no C}^{18}\text{O data.} \quad (5)$$

In other words, we assume the planets without C¹⁸O data are like the eight we identified in Figure 1 with C¹⁸O data showing evidence for $t_{\text{double}} \sim t_{\text{age}}$ — we posit that all are actively accreting from their surrounding discs, and that none are being observed in a short-lived growth phase. We view the values of Σ_{gas} so computed as predictions for future observations.

Figure 2 shows in red the gas surface densities predicted by equation (5). The values range from 10^{-4} g/cm^2 to 1 g/cm^2 , with a factor of 2-10 uncertainty in any given system stemming from the adopted range of planet masses M_p . Note that if $t_{\text{double}}/t_{\text{age}} > 1$, the red points shift down. Plotted in black for comparison are the Σ_{gas} values inferred from the measured C¹⁸O fluxes (same data plotted in the top panel of Figure 1). In some systems the Σ_{gas} predictions (red) overlap only with the lower end of values bracketed by the data (black) because $t_{\text{double}}/t_{\text{age}} = 1$ favors lower Σ_{gas} , as mentioned at the beginning of section 3.1.

The top panel of Figure 3 displays Σ_{dust} inferred from the mm continuum observations (section 2.2). The error bars account for a factor of 7 uncertainty in the grain opacity but not the potential overestimation of Σ_{dust} from gaps being inadequately resolved (more discussion on this below). In the bottom panel, we combine these values of Σ_{dust} with Σ_{gas} inferred from C¹⁸O data to plot, in black, the empirical dust-to-gas ratios $\Sigma_{\text{dust}}/\Sigma_{\text{gas}}$. The red points are semi-theoretical as they take Σ_{gas} from Figure 2 as predicted by equation (5).

The shaded bar $\Sigma_{\text{dust}}/\Sigma_{\text{gas}} < 10^{-1}$ in Figure 3 marks the range of dust-to-gas ratios found in simulated gaps (Dong et al. 2017). The simulations are initialized with spatially uniform dust-to-gas ratios near the solar value of $\sim 10^{-2}$. The ratios then evolve as aerodynamic drag causes dust to drift relative to gas. Across most of the gap, dust-to-gas ratios decrease as dust is diverted into local gas pressure maxima near gap edges. One gas pressure maximum coincides with the planet's orbit at gap center. Dust that collects in this co-orbital gas ring raises $\Sigma_{\text{dust}}/\Sigma_{\text{gas}}$ to ~ 0.1 (about ten times the solar value) for $M_p = 60 M_{\oplus}$ (Dong et al. 2017). Elsewhere within the gap, $\Sigma_{\text{dust}}/\Sigma_{\text{gas}} \ll 10^{-2}$. Such subsolar metallicities appear inconsistent with most of the data plotted in Figure 3.

The apparent disagreement between theory and observation could arise from some systematic error in M_p or h/r ($\Sigma_{\text{gas}} \propto M_p^{-1} (h/r)^4$ according to equation 5). It could also point to an error in the simulations' assumed initial condition of solar dust abundance. We think the most likely explanation is that the empirical values of Σ_{dust} are overestimated because the dust gaps are underresolved. Figure 3 suggests the measurement error in Σ_{dust} is at least a factor of 10-100. Errors of this magnitude are not necessarily surprising given how steep dust gradients can be in the simulations, especially for $M_p > 10 M_{\oplus}$ (Dong et al. 2017, third row of their figure 8). Indeed Jennings et al. (2021, their figure 12) re-analyzed the DSHARP data and found deeper bottoms to the dust gaps in GW Lup, SR 4, AS 209-G1, HD 143006-G1, and HD 163296-G2, in many instances by orders of magnitude relative to Huang et al. (2018).

3.3 Accretion luminosities, and the spectral energy distributions of the PDS 70 planets

From the average accretion rate $\dot{M}_p = M_p/t_{\text{age}}$ we can predict the bolometric accretion luminosities of planets in our sample (e.g. Frank et al. 2002):

$$L_{\text{acc}} = \frac{GM_p \dot{M}_p}{R_p}. \quad (6)$$

For the non-PDS 70 planets, we take radii R_p to be $R_J (M_p/M_J)^{-1/3}$ for $M_p > M_J$ and $R_J (M_p/M_J)^{1/3}$ for $M_p < M_J$. These scalings apply to planets that have finished cooling and contracting (e.g. Ginzburg & Chiang 2019b) and therefore probably underestimate R_p . We fix $R_p = 2 R_J$ for the PDS 70 planets, following fits by Wang et al. (2020) to the observed near-infrared photometry.⁵

Figure 4 also marks in blue the observed luminosities of PDS 70b and c at the short wavelengths thought to characterize the hot accretion shock. For PDS 70b, Zhou et al. (2021) estimated $L_{\text{acc}} = 1.8 \times 10^{-6} L_{\odot}$ from the measured U-band (336 nm) and H α

⁵ Wang et al. (2020) derived these radii by fitting blackbodies to the near-infrared spectral energy distributions of PDS 70b and c assuming no extinction. The radii may change by order-unity factors if there is circumplanetary extinction, as proposed later in this section.

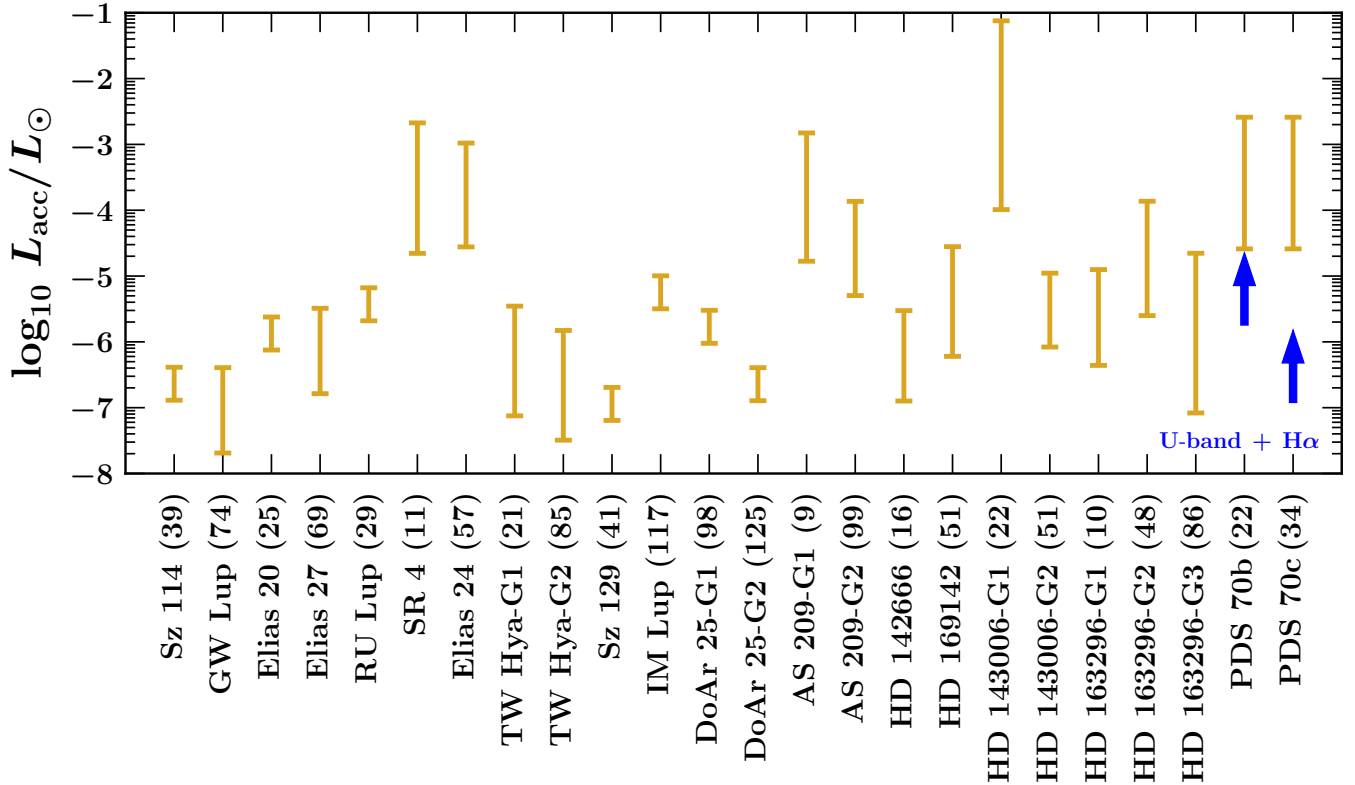


Figure 4. Predicted bolometric accretion luminosities $L_{\text{acc}} = GM_p \dot{M}_p / R_p$ assuming each planet is accreting at the average rate given by its mass and system age $\dot{M}_p = M_p / t_{\text{age}}$ (equivalently $t_{\text{double}} = t_{\text{age}}$). For the non-PDS 70 planets we estimate $R_p = R_J (M_p / M_J)^{1/3}$ for $M_p < M_J$ and $R_p = R_J (M_p / M_J)^{-1/3}$ for $M_p > M_J$. For PDS 70b and c we use $R_p = 2 R_J$ following blackbody fits by Wang et al. (2020) to near-infrared photometry. Error bars reflect the adopted range of M_p (see Table 1 or the top panel of Figure 2), including the dependence of R_p on M_p . The blue arrows show estimates of L_{acc} for the PDS 70 planets derived from observed U-band (336 nm) and H α fluxes. These values are hard lower limits because the accretion fluxes may be attenuated by dust along the line of sight, or the accretion luminosity may be concentrated in wavebands other than those observed. Figures 5 and 6 showing the SEDs for PDS 70b and c suggest much of the accretion power ultimately emerges in the infrared.

luminosities. This value includes a bolometric correction for the hydrogen continua, calculated using a slab model (Valenti et al. 1993) having parameters similar to those estimated for the accretion shock (Aoyama & Ikoma 2019). PDS 70c has so far only been detected in H α emission (Hashimoto et al. 2020), so we conservatively set $L_{\text{acc}} = L_{\text{H}\alpha} = 1.2 \times 10^{-7} L_{\odot}$. Figure 4 shows that these luminosities (in blue) sit a factor of ~ 100 below our estimates based on the time-averaged \dot{M}_p (in yellow).

There are at least two ways to reconcile our theorized high accretion luminosities for PDS 70b and c with the low short-wavelength luminosities observed to date. One possibility is that the bulk of the accretion luminosity emerges in as yet unobserved wavebands. In the accretion shock model of Aoyama et al. (2021), most of the power comes out in the hydrogen Lyman- α emission line. Their model for PDS 70b predicts a total accretion luminosity $L_{\text{acc}} \approx 5 \times 10^{-5} - 5 \times 10^{-4} L_{\odot}$ (see their figure 1). Alternatively, the observed U-band and H α fluxes may be highly attenuated by dust and therefore underestimate L_{acc} when not corrected for extinction (Hashimoto et al. 2020). These two explanations are not mutually exclusive; reality could be some combination of high dust extinction and high Lyman- α luminosity. In either scenario the true L_{acc} could be $\geq 10^{-4} L_{\odot}$, compatible with our Bondi accretion rate estimates.

We illustrate in Figures 5 and 6 how these two possibilities impact our interpretation of the spectral energy distributions (SEDs) of PDS 70b and c. Figure 5 describes the no-extinction case. Here the short-

wavelength luminosity generated from the accretion shock is $L_{\text{acc}} \sim 10^{-4} L_{\odot}$, released mostly in some unobserved waveband, possibly H Ly α (Aoyama et al. 2021). That the observed luminosity in the near-infrared (see tables 3 and 4 of Wang et al. 2020) is comparable to our predicted L_{acc} may not be a coincidence. Most of the near-infrared power may derive from the half of the radiation generated in the shock that is emitted toward and re-processed by cooler (10^3 K) layers below the shock (see Aoyama et al. 2020 for a model that details how the accretion power is re-processed).

In this extinction-free scenario the observed fluxes from the ultraviolet to the near-infrared are not significantly extinguished by dust. At the same time we know the circumplanetary environment should contain dust to explain the mm-wave continuum emission imaged by Isella et al. (2019) and Benisty et al. (2021). For this mm-bright dust to not obscure our line of sight to the planet, it should be distributed in a circumplanetary disc (CPD), viewed face on or approximately so. Figure 5 shows blackbody emission from a single-temperature CPD, heated primarily by radiation from the star to an assumed $T = 60$ K, with a radius fitted to the mm-wave observations. The fitted CPD radius is 0.3 au, roughly 20% of the Hill sphere radius $R_{\text{Hill}} \sim 1.5$ au $(M_p / M_J)^{1/3} (r / 22$ au).

Figure 6 shows a high-extinction scenario. Wang et al. (2020) ruled out interstellar extinction because the host star appears unextinguished, and circumstellar extinction seems negligible because the planets reside within a transitional disc cavity. Thus we are left with circum-

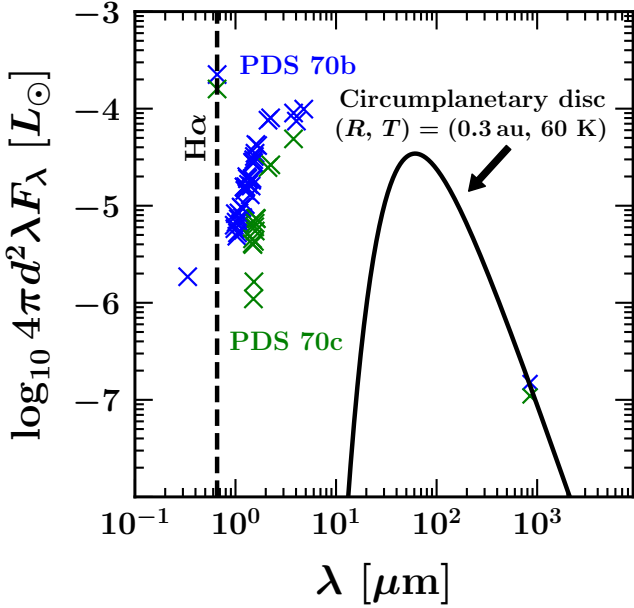


Figure 5. Observed SEDs of the PDS 70 planets (crosses) and emission from a single-temperature blackbody modeling a circumplanetary disc (CPD, black curve). Wavelength is denoted by λ , flux density by F_λ (units of energy per time per area per wavelength), and $d = 113$ pc is the source distance. The observed SEDs range from the U-band continuum and $H\alpha$ line (Hashimoto et al. 2020; Zhou et al. 2021), to the near-infrared (Müller et al. 2018; Mesa et al. 2019; Wang et al. 2020; Stolker et al. 2020; Wang et al. 2021), to the sub-mm (Isella et al. 2019; Benisty et al. 2021). The CPD temperature equals that of the local background nebula (60 K; section 2.3) and is assumed to be viewed face-on with a radius R chosen to match the observed mm-wave fluxes. Mass accretion rates calculated assuming Bondi accretion yield ultraviolet/optical accretion luminosities of order $10^{-4} L_\odot$, much higher than implied by the observed U-band flux (leftmost cross). Most of the accretional energy may be released instead as Lyman- α photons (Aoyama et al. 2020, 2021).

planetary extinction, from dust brought to the planet by the nebular accretion flow, pervading the planet’s Hill sphere. To obscure our line of sight to the accretion shock, this dust should be distributed more-or-less spherically around the planet, in a geometry similar to the thick torii found in 3D hydro-simulations by Fung et al. (2019, see their figure 2). The left panels of Figure 6 demonstrate how Hill-sphere-sized dusty spheres/torii can reproduce the measured sub-mm fluxes.

The right panels of Figure 6 show what the extinction-corrected intrinsic SED of the accreting planet might look like. We adopt power laws for how the extinction A_λ varies with wavelength λ , with the slope and normalization chosen such that the extinction-corrected luminosity in the U-band + $H\alpha$ is comparable to the extinction-corrected luminosity in the near-infrared, with both summing to an assumed bolometric luminosity L_{bol} ($10^{-4} L_\odot$ for the bottom panels, $10^{-3} L_\odot$ for the top; see the figure annotations and caption for details). Our V-band extinction for PDS 70b is $A_V \approx 2.5$ for $L_{\text{bol}} = 10^{-4} L_\odot$, and $A_V \approx 4$ for $L_{\text{bol}} = 10^{-3} L_\odot$. The de-reddened near-infrared SEDs still conform approximately to blackbodies, about as well as they do without any extinction correction applied (cf. Wang et al. 2020). Our extinction-corrected effective temperatures are higher than non-corrected values, $\sim 1100\text{--}1450$ K vs. $1000\text{--}1200$ K. Our corrected planet radii are also larger, $2.4\text{--}4.5 R_J$ vs. $2\text{--}2.7 R_J$. In

this interpretation the extinction-corrected near-infrared radius corresponds to the depth at which radiation emitted by the accretion shock boundary layer thermalizes, at the base of a dusty accretion flow. The analogy would be with actively accreting Class 0 protostars (e.g. Dunham et al. 2014) or “first” or “second” protostellar cores (Larson 1969; Bate et al. 2014) at the centres of infalling dusty envelopes.

4 SUMMARY AND OUTLOOK

Planets are suspected to open the gaps and cavities imaged in protoplanetary discs at millimeter and infrared wavelengths. From the literature we have compiled the modeled masses M_p and orbital radii r of the putative gap-opening planets, together with local disc properties including the dust and gas surface densities Σ_{dust} and Σ_{gas} , and the gas disc thickness h . Our sample contains 22 hypothesized planets and 2 confirmed orbital companions (PDS 70b and c). From these data we have evaluated:

(i) Present-day planetary gas accretion rates \dot{M}_p for the subset of 9 planets (including PDS 70b and c) for which the ambient gas density can be usefully constrained from molecular line observations including optically thin C^{18}O . We assumed, consistent with some theories of planet formation, that accretion from the surrounding disc onto the planet is Bondi-like. For 8 of the 9 planets, accretion rates are such that mass doubling times $t_{\text{double}} \equiv M_p/\dot{M}_p$ are comparable to stellar ages of $t_{\text{age}} \sim 1\text{--}10$ Myr — this assumes the non-PDS 70 planets have masses $M_p \sim 10\text{--}30 M_\oplus$, the PDS 70 planets have $M_p \sim 1\text{--}10 M_J$, and the gas-phase CO:H_2 abundance ratios are close to those found in thermo-chemical models. Since circumstellar gas discs have typical lifetimes of several Myr, our finding that $t_{\text{double}}/t_{\text{age}} \sim 1$ for these 8 planets suggests we are observing them during their last doublings. The one planet that does not fit this pattern is the one supposedly inside HD 163296-G2 ($r = 48$ au), for which we find $t_{\text{double}}/t_{\text{age}} \lesssim 0.1$ if $M_p \sim 1\text{--}10 M_J$ as estimated by Zhang et al. (2018). We suggest the true planet mass in this gap is smaller, and could actually be zero if the gap is created by a planet located elsewhere, following Dong et al. (2018).

(ii) Gas surface densities Σ_{gas} at the bottoms of 24 gaps where planets are supposed to reside. For 9 systems we compiled literature estimates of Σ_{gas} based on observed C^{18}O intensity maps. For the remaining 15 systems we inferred Σ_{gas} assuming the gaps host planets undergoing Bondi accretion at the average rate \dot{M}_p/t_{age} . The predicted gas surface densities range from 10^{-4} g/cm^2 to 1 g/cm^2 .

(iii) Dust surface densities Σ_{dust} and dust-to-gas ratios $\Sigma_{\text{dust}}/\Sigma_{\text{gas}}$ inside gaps. In many cases $\Sigma_{\text{dust}}/\Sigma_{\text{gas}}$ based on observations are supersolar, by contrast to the typically subsolar ratios found at the bottoms of dust-filtered gaps in planet-disc simulations (Dong et al. 2017). We suggest Σ_{dust} may be overestimated by the current ALMA observations as they may not be resolving steep dust gradients inside gaps (see also Jennings et al. 2021). Under-resolution is less of a problem for Σ_{gas} insofar as simulations predict gas gradients to be shallower than dust gradients.

(iv) Accretion luminosities L_{acc} of protoplanets. For the PDS 70 planets we predict $L_{\text{acc}} \sim 10^{-4} L_\odot$, a factor of 10-100 larger than observed in the U-band and $H\alpha$. Most of the short-wavelength accretion power might be emitted in wavebands as yet unobserved, e.g. H Lyman- α as predicted by recent accretion shock models (Aoyama et al. 2021). Alternatively, a dusty, quasi-spherical, circumplanetary envelope might be absorbing much of the outgoing ultraviolet/optical radiation. We sketched different spectral energy distributions (SEDs)

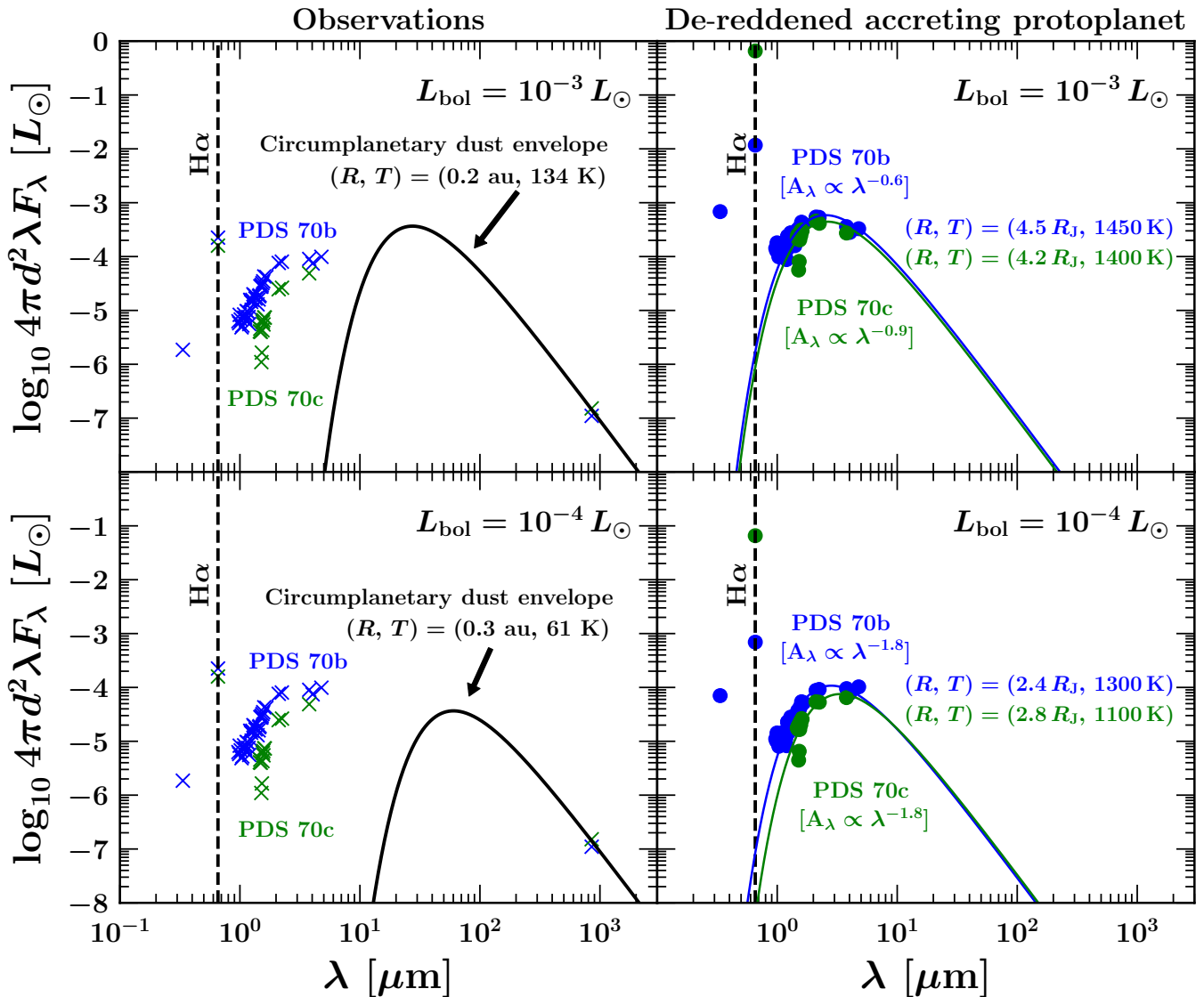


Figure 6. Similar to Figure 5, but now modeling the case where the PDS 70 planets are surrounded by dusty spherical envelopes instead of circumplanetary discs. Crosses in the left panels mark the observed SEDs, identical to those in Figure 5. In the right panels we show these data de-reddened, adopting a power-law extinction curve chosen so that the extinction-corrected luminosity in the U-band + H α is comparable to that in the near-infrared, with both summing to a given bolometric luminosity L_{bol} ($10^{-4}L_{\odot}$ for the bottom panels, $10^{-3}L_{\odot}$ for the top). These choices are intended to describe protoplanets which derive a large fraction of their luminosity from ongoing accretion, producing short-wavelength ultraviolet/optical radiation in an accretion shock that heats the planetary layers below and the circumplanetary envelope above. The blackbody fits to the de-reddened near-infrared SEDs (right panels) suggest the accretion shock lies just above $\sim 2\text{--}5 R_{\text{J}}$. The circumplanetary envelope intercepts nearly all of the outgoing radiation and re-radiates it longward of $10\text{--}30 \mu\text{m}$ wavelength on size scales comparable to the Hill sphere, as shown by the blackbodies with luminosities equal to L_{bol} running through the mm-wave fluxes (left panels). The large de-reddened U-band and optical luminosities in this figure (10^{-4} , $10^{-3}L_{\odot}$) are consistent with planetary accretion at Bondi-like rates and mass doubling times t_{double} comparable to the system age t_{age} .

based on these scenarios. A large fraction of the power is expected to emerge at wavelengths ranging from the mid to far-infrared.

The hypothesis that the disc substructures imaged by ALMA are caused by embedded planets is now supported on several grounds. A planet can reproduce the observed positions of multiple gaps in a given system (e.g. in AS 209; Dong et al. 2017, 2018; Zhang et al. 2018). A planet can also reproduce observed non-Keplerian velocity signatures in the disc rotation curve (e.g. in HD 163296; Teague et al. 2018, 2021; Pinte et al. 2020). To this evidence favoring planets we can now add consistency with planet accretion theory. The data are

pointing to Neptune-mass planets accreting at Bondi-like rates inside gaps filled with low-viscosity ($\alpha \lesssim 10^{-4}$) gas.

From here there are any number of avenues for future investigation. To list just a few:

- (i) Advancing beyond our Bondi-inspired formula (3) for \dot{M}_{p} . Bondi accretion neglects many effects, among them stellar tides that become important when the planet’s Bondi radius exceeds its Hill radius (e.g. Rosenthal et al. 2020), anisotropic 3D flow fields (e.g. Cimerman et al. 2017), and thermodynamics (e.g. Ginzburg & Chiang 2019a who distinguished between hydrodynamic and thermo-

dynamic runaway). The sensitivity of simulated accretion rates to sink-cell (e.g. D'Angelo et al. 2003) and other planetary boundary conditions should be studied.

(ii) Accounting for how the gap density evolves with time because of disc photoevaporation, repulsive planetary torques, etc., while the planet accretes. For example, in the gap clearing theories of Ginzburg & Chiang (2019a), the planet mass doubling timescale t_{double} is longer than the instantaneously measured M_p/\dot{M}_p by a factor that ranges up to ~ 15 , increasing as the disc viscosity decreases and the gap depletes more rapidly with time. This correction factor based on disk evolution should be incorporated into comparisons between t_{double} and t_{age} .

(iii) More molecular line data to test our predictions for Σ_{gas} , and higher spatial resolution to map steep Σ_{dust} profiles. New data are now available for the GM Aur disc, including spatially resolved dust continuum and CO observations (Huang et al. 2020, 2021; Schwarz et al. 2021), anchored by a total disc gas mass estimate from HD emission (McClure et al. 2016). Spatially resolved disc surveys have so far targeted brighter discs (Andrews et al. 2018; Oberg et al. 2021) and are consequently biased toward higher Σ_{gas} . Assuming planets will always be found with $t_{\text{double}}/t_{\text{age}} \gtrsim 1$, higher Σ_{gas} corresponds to lower planet masses M_p (equation 5). By this logic, targeting less luminous, less massive discs while keeping all other factors fixed may uncover higher mass planets. In any case expanding survey samples are necessary for understanding planet occurrence rates and demographic trends (Cieza et al. 2019).

(iv) Planetary accretion shock models (Aoyama et al. 2020, 2021) need to be tested observationally across the ultraviolet-optical spectrum, with current arguments based on a single emission line (H α) replaced by joint constraints from multiple lines and the continuum. The accretion shock theory also needs to connect more smoothly to models of the cooler, infrared-emitting layers of the planet (e.g. BT-Settl; Baraffe et al. 2015); at the moment how radiation from shocked layers heats cooler layers is not accounted for (but see section A1 of Aoyama et al. 2020 for a first step). Detection of molecular absorption lines in the infrared (Cugno et al. 2021; Wang et al. 2021) may constrain the degree of accretional heating, and how much dust is brought in.

ACKNOWLEDGEMENTS

We thank Yuhiko Aoyama, Steve Beckwith, Jenny Calahan, Yayaati Chachan, Ruobing (Robin) Dong, Jeffrey Fung, Sivan Ginzburg, Jane Huang, Masahiro Ikoma, Gabriel-Dominique Marleau, Jason Wang, Ke (Coco) Zhang, Shangjia Zhang, Yifan Zhou, and Zhaohuan Zhu, for discussions and feedback on our study. We also thank Takayuki Muto for a helpful referee report. This work was supported by an NSF Graduate Research Fellowship (DGE 2146752) and used the MATPLOTLIB (Hunter 2007) and SCIPY (Virtanen et al. 2020) packages.

DATA AVAILABILITY

The data compiled in this work are available upon request to the authors.

REFERENCES

ALMA Partnership et al., 2015, *ApJ*, 808, L3
 Alarcón F., et al., 2021, arXiv e-prints, arXiv:2109.06263
 Andrews S. M., 2020, *ARA&A*, 58, 483

Andrews S. M., et al., 2016, *ApJ*, 820, L40
 Andrews S. M., et al., 2018, *ApJ*, 869, L41
 Aoyama Y., Ikoma M., 2019, *ApJ*, 885, L29
 Aoyama Y., Marleau G.-D., Mordasini C., Ikoma M., 2020, arXiv e-prints, arXiv:2011.06608
 Aoyama Y., Marleau G.-D., Ikoma M., Mordasini C., 2021, *ApJ*, 917, L30
 Asensio-Torres R., et al., 2021, *A&A*, 652, A101
 Baraffe I., Homeier D., Allard F., Chabrier G., 2015, *A&A*, 577, A42
 Bate M. R., Tricco T. S., Price D. J., 2014, *MNRAS*, 437, 77
 Benisty M., et al., 2021, *ApJ*, 916, L2
 Binkert F., Szulágyi J., Birnstiel T., 2021, *MNRAS*, 506, 5969
 Birnstiel T., et al., 2018, *ApJ*, 869, L45
 Blondel P. F. C., Djie H. R. E. T. A., 2006, *A&A*, 456, 1045
 Bruderer S., 2013, *A&A*, 559, A46
 Calahan J. K., et al., 2021, *ApJ*, 908, 8
 Chachan Y., Lee E. J., Knutson H. A., 2021, arXiv e-prints, arXiv:2101.10333
 Chiang E. I., Goldreich P., 1997, *ApJ*, 490, 368
 Christiaens V., Cantalloube F., Casassus S., Price D. J., Absil O., Pinte C., Girard J., Montesinos M., 2019, *ApJ*, 877, L33
 Cieza L. A., et al., 2019, *MNRAS*, 482, 698
 Cimerman N. P., Kuiper R., Ormel C. W., 2017, *MNRAS*, 471, 4662
 Cugno G., et al., 2021, *A&A*, 653, A12
 D'Angelo G., Kley W., Henning T., 2003, *ApJ*, 586, 540
 Dong R., Fung J., 2017, *ApJ*, 835, 146
 Dong R., Li S., Chiang E., Li H., 2017, *ApJ*, 843, 127
 Dong R., Li S., Chiang E., Li H., 2018, *ApJ*, 866, 110
 Drążkowska J., Li S., Birnstiel T., Stammerl S. M., Li H., 2019, *ApJ*, 885, 91
 Du F., Bergin E. A., 2014, *ApJ*, 792, 2
 Ducourant C., Teixeira R., Galli P. A. B., Le Campion J. F., Krone-Martins A., Zuckerman B., Chauvin G., Song I., 2014, *A&A*, 563, A121
 Dunham M. M., et al., 2014, in Beuther H., Klessen R. S., Dullemond C. P., Henning T., eds, *Protostars and Planets VI*. p. 195 (arXiv:1401.1809), doi:10.2458/azu_uapress_9780816531240-ch009
 Facchini S., Teague R., Bae J., Benisty M., Keppler M., Isella A., 2021, *AJ*, 162, 99
 Favre C., et al., 2019, *ApJ*, 871, 107
 Fedele D., et al., 2017, *A&A*, 600, A72
 Flaherty K. M., et al., 2017, *ApJ*, 843, 150
 Frank J., King A., Raine D. J., 2002, *Accretion Power in Astrophysics: Third Edition*. Cambridge University Press
 Fung J., Zhu Z., Chiang E., 2019, *ApJ*, 887, 152
 Ginzburg S., Chiang E., 2019a, *MNRAS*, 487, 681
 Ginzburg S., Chiang E., 2019b, *MNRAS*, 490, 4334
 Ginzburg S., Schlichting H. E., Sari R., 2016, *ApJ*, 825, 29
 Goldreich P., Tremaine S., 1979, *Nature*, 277, 97
 Gregory S. G., Jardine M., Simpson I., Donati J. F., 2006, *MNRAS*, 371, 999
 Guidi G., et al., 2018, *MNRAS*, 479, 1505
 Guzmán V. V., et al., 2018, *ApJ*, 869, L48
 Haffert S. Y., Bohn A. J., de Boer J., Snellen I. A. G., Brinchmann J., Girard J. H., Keller C. U., Bacon R., 2019, *Nature Astronomy*, 3, 749
 Hashimoto J., Aoyama Y., Konishi M., Uyama T., Takasao S., Ikoma M., Tanigawa T., 2020, *AJ*, 159, 222
 Huang J., et al., 2018, *ApJ*, 869, L42
 Huang J., et al., 2020, *ApJ*, 891, 48
 Huang J., et al., 2021, arXiv e-prints, arXiv:2109.06224
 Hunter J. D., 2007, *Computing In Science & Engineering*, 9, 90
 Isella A., et al., 2016, *Phys. Rev. Lett.*, 117, 251101
 Isella A., Benisty M., Teague R., Bae J., Keppler M., Facchini S., Pérez L., 2019, *ApJ*, 879, L25
 Jennings J., Booth R. A., Tazzari M., Clarke C. J., Rosotti G. P., 2021, arXiv e-prints, arXiv:2103.02392
 Jorquera S., et al., 2021, *AJ*, 161, 146
 Keppler M., et al., 2018, *A&A*, 617, A44
 Keppler M., et al., 2019, *A&A*, 625, A118
 Larson R. B., 1969, *MNRAS*, 145, 271
 Lee E. J., Chiang E., 2015, *ApJ*, 811, 41
 Lodato G., et al., 2019, *MNRAS*, 486, 453

- Machida M. N., Kokubo E., Inutsuka S.-I., Matsumoto T., 2010, *MNRAS*, **405**, 1227
- Mangum J. G., Shirley Y. L., 2015, *PASP*, **127**, 266
- McClure M. K., et al., 2016, *ApJ*, **831**, 167
- Mesa D., et al., 2019, *A&A*, **632**, A25
- Müller A., et al., 2018, *A&A*, **617**, L2
- Nomura H., et al., 2021, *ApJ*, **914**, 113
- Oberg K. I., et al., 2021, arXiv e-prints, [arXiv:2109.06268](https://arxiv.org/abs/2109.06268)
- Paardekooper S. J., Mellema G., 2004, *A&A*, **425**, L9
- Pinte C., Dent W. R. F., Ménard F., Hales A., Hill T., Cortes P., de Gregorio-Monsalvo I., 2016, *ApJ*, **816**, 25
- Pinte C., et al., 2020, *ApJ*, **890**, L9
- Pohl A., et al., 2017, *ApJ*, **850**, 52
- Qi C., D'Alessio P., Öberg K. I., Wilner D. J., Hughes A. M., Andrews S. M., Ayala S., 2011, *ApJ*, **740**, 84
- Quanz S. P., Avenhaus H., Buenzli E., Garufi A., Schmid H. M., Wolf S., 2013, *ApJ*, **766**, L2
- Rodenkirch P. J., Rometsch T., Dullemond C. P., Weber P., Kley W., 2021, *A&A*, **647**, A174
- Rosenthal M. M., Chiang E. I., Ginzburg S., Murray-Clay R. A., 2020, *MNRAS*, **498**, 2054
- Schwarz K. R., Bergin E. A., Cleeves L. I., Zhang K., Öberg K. I., Blake G. A., Anderson D., 2018, *ApJ*, **856**, 85
- Schwarz K. R., et al., 2021, arXiv e-prints, [arXiv:2109.06228](https://arxiv.org/abs/2109.06228)
- Shakura N. I., Sunyaev R. A., 1973, *A&A*, **500**, 33
- Stolker T., Marleau G. D., Cugno G., Mollière P., Quanz S. P., Todorov K. O., Kühn J., 2020, *A&A*, **644**, A13
- Tanigawa T., Tanaka H., 2016, *ApJ*, **823**, 48
- Teague R., et al., 2016, *A&A*, **592**, A49
- Teague R., Bae J., Bergin E. A., Birnstiel T., Foreman-Mackey D., 2018, *ApJ*, **860**, L12
- Teague R., et al., 2021, arXiv e-prints, [arXiv:2109.06218](https://arxiv.org/abs/2109.06218)
- Valenti J. A., Basri G., Johns C. M., 1993, *AJ*, **106**, 2024
- Virtanen P., et al., 2020, *Nature Methods*, **17**, 261
- Wang J. J., et al., 2020, *AJ*, **159**, 263
- Wang J. J., et al., 2021, *AJ*, **161**, 148
- Zhang S., et al., 2018, *ApJ*, **869**, L47
- Zhang K., Bergin E. A., Schwarz K., Krijt S., Ciesla F., 2019, *ApJ*, **883**, 98
- Zhang K., et al., 2021, arXiv e-prints, [arXiv:2109.06233](https://arxiv.org/abs/2109.06233)
- Zhou Y., et al., 2021, *AJ*, **161**, 244
- van Boekel R., et al., 2017, *ApJ*, **837**, 132
- van der Marel N., van Dishoeck E. F., Bruderer S., Pérez L., Isella A., 2015, *A&A*, **579**, A106

This paper has been typeset from a $\text{\TeX}/\text{\LaTeX}$ file prepared by the author.